Connectome of a human foveal retina

Yeon Jin Kim[1], Orin Packer[1], Thomas Macrina[2], Andreas Pollreisz[3], Christine A. Curcio[4], Kisuk Lee[2], Nico Kemnitz[2], Dodam Ih[2], Tri Nguyen[2], Ran Lu[2], Sergiy Popovych[2], Akhilesh Halageri[2], J. Alexander Bae[2], Joseph J. Strout[2], Stephan Gerhard[5], Robert G. Smith[6], Paul R. Martin[7], Ulrike Grünert[7], Dennis M. Dacey[1,8,*]

[1]Department of Neurobiology & Biophysics, University of Washington, Seattle, WA, 98195

[2]Zetta AI LLC, Sherrill, NY, USA

[3]Department of Ophthalmology, Medical University of Vienna, Vienna, Austria

[4]Department of Ophthalmology and Vision Sciences, University of Alabama at Birmingham, Alabama 35294

[5]Aware LLC, Rappenstrasse 19, 8307 Effretikon, Switzerland

[6]Department of Neuroscience, University of Pennsylvania, Philadelphia, PA 19104

[7]The University of Sydney, Save Sight Institute and Discipline of Ophthalmology, Faculty of Medicine and Health, Sydney, NSW, 2000, Australia

[8]Washington National Primate Research Center, Seattle, WA 98195

*Corresponding author: Dennis M. Dacey (dmd@uw.edu)

This file includes:

Main Text (Main text pages: 17, Total pages: 50)

Figures 1 to 8

Abstract

What makes human brains distinctive? The answer is hidden at least partially in the myriad synaptic connections made between neurons – the connectome. The foveal retina is a primate specialization which presents a feasible site for deriving a complete connectome of a human CNS structure. In the fovea, cells and circuits are miniaturized and compressed to densely sample the visual image at highest resolution and initiate form, color and motion perception. Here we provide a draft connectome of all neurons in a human fovea. We found synaptic connections, distinct to humans, linking short-wavelength sensitive cones to color vision pathways. Moreover, by reconstructing excitatory synaptic pathways arising from cone photoreceptors we found that over 95% of foveal ganglion cells contribute to only three major pathways to the brain. Our study reveals unique features of a human neural system and opens a door to a complete foveal connectome.

Main

The vertebrate retina, an accessible central nervous system (CNS) outpost where the visual process starts, has long been appreciated for its great complexity[1] and for linking neural structure to visual function[2-4]. The retina was also an early focus of synaptic level connectomic reconstruction[5-10], and more recently, retinal cell populations have also been linked to their molecular profiles[11-14] and the genetics of human disease[13, 15]. Yet even for this intensively studied neural system, we lack a full wiring diagram that could explain how one of our most fundamental senses – vision – is initiated.

The recent achievement of a complete connectome of the brain of the fruit fly, Drosophila melanogaster[16, 17], has made the connectome of a larger mammalian brain a now-conceivable goal[18-21] and connectomic methods have recently been applied to mm-scale volumes of mouse and human neocortex[19, 20, 22, 23]. In the present study we take advantage of the distinctive neural architecture of the foveal retina, to provide a first draft connectome of this critical locus in the human CNS.

The fovea is a specialized central region in the retina of humans and other day-active primates where neural circuits are spatially compressed to facilitate high resolution form, color and motion perception. At barely 1 mm wide the fovea encodes only a few degrees of visual space, but its representation is magnified 100-fold across the surface of primary visual cortex[24-28]. Accordingly, the fovea is essential for normal vision, and failure of foveal function is a hallmark of devastating blinding retinal diseases.

From a signal-processing viewpoint, the fovea is a self-contained input-to-output sensory structure, where light transduction by photoreceptors is processed by diverse neural cell types across two narrow cell and synaptic layers. Here we provide a catalog of human foveal cells as well as assignment of synaptic connections to distinct functional circuits. We use this dataset to

directly address the long-standing question of the number and identity of visual pathways that link the fovea to the brain. We find only three visual pathways account for over 95% of the eye's projection to the human brain: a striking reduction compared to both non-primate mammals[29-31] and non-human primates[32, 33]. In addition, we observed unexpected differences in synaptic connections compared to non-human primates and provide evidence that neural coding for trichromatic color vision begins with circuitry that is uniquely human.

Results

Acquisition of the foveal volume. Our goal was to obtain complete retinal circuitry near the peak of cone density (peak of visual acuity)[34, 35]. This is a difficult task because (among other reasons) foveal cones feed inner retinal circuits via very long axons (Henle fibers, Fig. 1a-1c)[36]. Our data sample therefore was centered at 500 µm retinal eccentricity, where cone axon length averages 300 µm[37]; this location is linked to cones located ~200-300 µm from the center of the foveal pit (~0.7-1 deg). We cut 3028 vertical sections at 50 nm through a depth of ~150 µm and imaged an area that was 180 µm tall x 180 µm wide at 5 nm resolution (voxel size, 5x5x50 nm^3), extending from the Henle fiber layer (outer retina) to the nerve fiber layer (inner retina) (Fig. 1d). Recently developed computational methods (convolutional neural networks)[38, 39] were used to align the images, detect membrane boundaries, segment neurons, glia, blood vessels, simple (conventional) and complex (ribbon) synapses, and predict synaptic relationships in the outer and inner synaptic layers (Fig. 1d-1k; see Methods for procedures). For ease of reference, we named this volume HFseg1 (Human Fovea, segmented 1). All annotated cell types and the draft catalog of synaptic connections are available for exploration using search tools in an openly accessible form (https://neuromaps.app/datasets, see Supplementary Data Table 3) which utilizes the Neuroglancer browser and CAVE infrastructure. In addition, we have created a second site (accessed via NeuroMaps) that facilitates directed proofreading of both cells and synapses by a user community.

Cell populations

To derive and understand any connectome, the identity and layout of all cell types must first be clearly understood. Here, we took advantage of a well-established morphology of the majority of foveal cell types[40, 41] that have also been linked to transcriptomically defined cell clusters in both human and non-human primate retina[12, 13, 42]. Moreover, for many cell populations the

presence of orderly spatial arrays and their distinctive morphology could be used to define not only a cell type but its relative density. We were therefore able to use the original segmentation followed by proofreading of cell morphology (~37,000 edits to date) to annotate and classify all cells by class and specific type and to assess the quality of synapse prediction (Fig. 1f-1g; see Supplementary Data Table 1a, 3008 total cells with annotated cell bodies and ~368,000 total synapses).

In brief, HFseg1 contained 313 cone (pedicles) and 24 rod (spherules) synaptic terminals (rod: cone = 0.07, Supplementary Data Table 1c, 1d). Sixteen cone pedicles were identified as short wavelength sensitive (S) cones (Supplementary Data Table 1c; Fig. 2a)[43]. The remaining 297 cones comprised long (L) and medium (M) wavelength sensitive cones, here referred to collectively as LM cones. Postsynaptic to cones were 268 horizontal cells and 912 bipolar cells (Supplementary Data Table 1e, 1f). It was possible to distinguish the H1 and H2 horizontal cell types by distinctive morphology and connectivity (Fig. 2) and most of the classically recognized bipolar cell types (midget and diffuse bipolar types). Some exceptions will be considered further below (Fig. 3).

We annotated 293 amacrine cells, including 40 cells displaced to the ganglion cell layer (Supplementary Data Table 1g, Figs. 4, 5; Extended Data Figs. 6, 8), first dividing cells by dendritic field diameter into small (diameter < 100 μm; n = 189), and large field (diameter >100 μm) groups (n = 104). We divided these groups in turn into 19 types (6 small field and 13 large field; Supplementary Data Table 1g) based on morphology, stratification, mosaic interactions and nuclear morphology (Extended Data Figs. 3, 6, 8). Figure 4 provides a partial view of this dataset by highlighting four cell types (see also Supplementary Data Table 3); two additional amacrine populations are illustrated in Extended Data Figure 8 and others can be viewed at the NeuroMaps site.

121 We annotated 599 ganglion cell bodies (Fig. 1g; Supplementary Data Table 1h). As expected,
122 the classically recognized midget GCs constitute the great majority (536 cells, ~90%,
123 Supplementary Data Table 1h)[13, 44]; these were readily divided into outer-OFF stratifying (280
124 cells) and inner-ON stratifying (256 cells) types (Fig. 7a, 7e). A second well defined cell group,
125 the parasol cells (26 cells, 13 inner-ON cells and 13 outer-OFF cells, ~4% of total GCs) was
126 also easily distinguished (Fig. 7b, 7f; Supplementary Data Table 1h). Small bistratified GCs[45],
127 found to show blue-yellow color opponency in macaque retina[46, 47] were distinguished by their
128 broad dendritic ramification (12 cells, ~2% of total GCs, Supplementary Data Table 1h; Fig. 7c,
129 7g) and extensive synaptic input from blue cone bipolar cells (BB cells)[48]. Together, the midget,
130 parasol and small bistratified cells accounted for 95.8% of the ganglion cells in HFseg1
131 (Supplementary Data Table 1h). The remaining 25 ganglion cells showed relatively large
132 dendritic fields and were divided provisionally into five types (Supplementary Data Table 1h,
133 Supplementary Notes) pending a more detailed analysis of their synaptic connections.

134 Lastly, glial cells were readily distinguished from all neurons by their distinctive ultrastructure
135 (Extended Data Fig. 3a, 3b, 3c, 3f). The Müller cells (555 cells, Fig. 1g; Supplementary Data
136 Table 1b) were distinguished as radial glia with cell bodies in the inner nuclear layer (Extended
137 Data Fig. 1a). A second, morphologically distinct population of glial cells in the GCL was
138 closely associated with the superficial blood vessels there (Extended Data Figs. 1b and 3b)
139 and provisionally identified as astrocytes[49] (32 cells, Supplementary Data Table 1b; Extended
140 Data Fig. 1b). We also identified 15 microglial cells (Supplementary Data Table 1b) with cell
141 bodies in the IPL or GCL (Extended Data Fig. 1a) distinct from both Müller cells and astrocytes
142 (Extended Data Figs. 1a, 1b and 3c, 3b; Fig. 1f). The density of microglial cells was low,
143 consistent with previous measurements in the macaque monkey foveal retina[50, 51]. In the
144 current volume we have not yet attempted to characterize blood vessel and associated
145 pericytes, though these cellular elements are also segmented and are available to annotate

146 and further characterize. More detailed information on cell type identification is provided in a
147 supplement (Supplementary Notes on cell type identification).

148 **Synapse detection**

149 To assess the accuracy of ribbon segmentation and synapse prediction in HFseg1 (Fig. 1h-1k)
150 we compared deep-learning predicted synaptic assignments to manual (ground truth)
151 assignments. We focused on the cone-to-midget bipolar cell synapse in the OPL and the
152 midget bipolar cell synapses to amacrine and ganglion cells in the IPL. For ground truth, we
153 manually annotated all synaptic connections for the midget pathway connections to three LM
154 cones (cones 21, 22, and 58; Extended Data Fig. 9; Supplementary Data Table 2a-2c).

155 Figure 6 shows the predicted outgoing synapses for a pair of midget bipolar cell axon
156 terminals. Measures of precision (true synapses / [true synapses + false positives]) and
157 sensitivity (true synapses / [true synapses + false negatives]) were taken for ribbons and their
158 synapses. The segmentation of ribbons showed precision and sensitivity near 100% (n = 370
159 ribbons; n = 6 midget bipolar cells; precision: 93.5% ± 2.7%; sensitivity: 99.7% ± 0.8%, Fig. 6b
160 inset). Post-synaptic partner assignment for these ribbons was also excellent (n = 637
161 synapses; n = 6 midget bipolar cells; precision: 89.0% ± 5.4%; sensitivity: 93.7% ± 4.6%; Fig.
162 6b inset). These values demonstrate the high accuracy of convolutional nets for predicting and
163 segmenting ribbon synapses.

164 By contrast with the ribbon synapses made in the IPL, ribbon synapses made by the cone
165 pedicle in the OPL are extremely complex[52, 53] (Fig. 1h, 1i). Post-synaptic processes can either
166 invaginate into the face of the pedicle or occupy a basal position at the cone pedicle up to ~800
167 nm from the sites of transmitter release[53, 54]. We mapped all incoming cone synapses to the
168 dendritic tips for each of six midget bipolar cells sampled. We found high precision and
169 sensitivity for ribbon detection (n = 51 ribbons; n = 3 LM cones; precision: 92.3% ± 6.7%;

170 sensitivity: 100% ± 0%, Extended Data Fig. 2a-2c) and for the multiple postsynaptic processes
171 deriving from the invaginating (IMB) and flat (FMB) midget bipolar cells (n = 153 connections;
172 precision: 98.7% ± 1.2%; sensitivity: 99.7% ± 0.6%; see Extended Data Fig. 2c right). Diffuse
173 bipolar cells, which make more sparse connections with multiple cones, were also sampled (n
174 = 2, DB4 and DB2; Extended Data Fig. 2d-2f), yielding similar precision and sensitivity results.

175 For conventional synapses, we focused on the AII amacrine cell (Figs, 4a, 5, 6c;
176 Supplementary Data Table 1g) where an inhibitory glycinergic synapse to OFF bipolar cell
177 axon terminals is well established [55-58]. We manually mapped all the outgoing synapses made
178 by two neighboring AII amacrine cells and compared our ground truth data to the predicted
179 synaptic assignments (Fig. 6c-6g). The prediction captured well the origin of synaptic output
180 from the outer stratifying lobular appendages of the AII cell to outer-OFF bipolar cells (Fig. 6d-
181 6g). Vesicle clouds were also detected with high sensitivity (87.5% ± 0.7%, n = 2 AII cells; false
182 negatives were rare (Fig. 6c bottom) but relative to ribbon detection, there were more false
183 positives, thereby reducing the accuracy of the overall synapse detection (76.0% ± 8.5%, n = 2
184 AII cells). With this limitation, the results show that our dataset accurately reflects synaptic
185 connectivity.

186 The initial picture of the cell types and their synaptic connections in HFseg1 permitted us to ask
187 to what degree have cells and circuits become distinctive in human vs non-human primate.
188 Here we call attention to some examples where differences are dramatic and require further
189 study.

190 **Retinal connectivity and color vision: distinctive features of the S cone circuit**

191 Cone pedicles contact each other by short extensions (telodendria) or by distinct pedicle-to-
192 pedicle appositions (Fig. 2b). These contacts harbor gap junctions that create electrical
193 synapses between cones. In non-human primates, LM to LM cone contacts are abundant, but

194 S to LM contacts are greatly reduced or absent[43, 59]: this difference may reflect a need to
195 support color vision by isolating short from long wavelength signals[60, 61]. In human retina
196 however S-LM cone contacts have been reported[62, 63]. We therefore mapped the full cone-cone
197 connectome to determine whether S-LM contacts are a consistent feature of human fovea.
198 Cone-cone contacts (n = 1141) were characterized by a thick, darkly stained region defining
199 the contact area (see Fig. 2b insets)[64]. We found abundant S–LM cone contacts (n = 16 S
200 cones; 5.25 ± 2.11 contacts/S-cone pedicle), indistinguishable from LM–LM cone contacts (n =
201 297 LM cones; 6.89 ± 3.08 contacts/pedicle). The functional significance of this species
202 difference in cone-cone connectivity remains to be explored with biophysical modeling.
203 Nevertheless, these data predict that in human foveal retina S-LM cone gap junctions could
204 alter the spectral tuning of the S cone synaptic output.

205 A second difference in synaptic connectivity that may impact color vision occurs at the synapse
206 between cones and horizontal cell interneurons. The horizontal cell network in the outer retina
207 generates lateral negative feedback that underlies the antagonistic receptive field surround of
208 cones, bipolar cells, and ganglion cells[65]. In macaque monkey retina the horizontal cell
209 mediated surround is a key element in the circuitry that initiates red-green color vision[66-68]. In
210 both macaque and marmoset, H1 cells make dense contacts with LM cones but largely or
211 completely avoid contact with S cones, whereas H2 cells show some selectivity for S cones[69-
212 71]. While the H2 cells in HFseg1 did maintain a clear preference for synapsing with S cones
213 (Fig. 2d), we found that H1 cells also received a major input from S cones, comparable to H2
214 cells (H1, 43% ± 16%; H2, 57% ± 16%, n = 10 S cones). By contrast, H2 cells formed less than
215 2% of the horizontal cell contacts with LM cones (1.9% ± 0.1%, n = 2 LM cones; also Extended
216 Data Fig. 4). As a consequence, human foveal H1 cells are predicted to show a trichromatic
217 receptive field with a small S cone contribution (Fig. 2c, 2d; Extended Data Fig. 4). Taken
218 together, the S-LM cone coupling and the combined S and LM cone connectivity of H1

219 horizontal cells provides new connectomic evidence for a difference between human and non-
220 human primates in the circuits that initiate color vision[43], and that remains to be further
221 explored.

222 **Distinctive bipolar and amacrine cell circuits in HFseg1**

223 We found differences in both bipolar and amacrine cell circuits in HFseg1 compared to
224 expectations from macaque monkey, whereby some bipolar cell types were either greatly
225 reduced or absent. For example, in macaque monkey non-midget or diffuse (DB) OFF bipolar
226 cells can be divided into 4 types (DB 1, 2, 3a and 3b) but in HFseg1 we were only able to
227 distinguish three populations that we call DB1, 2 and 3. Bipolar cell morphologies not
228 previously described in primates were also present. One group showed amacrine-like
229 morphology (called here outer-x and inner-x in Fig. 3a, 3b) but contained abundant ribbon
230 synapses (20 cells, Supplementary Data Table 1f; Extended Data Fig. 6). Similar cells were
231 discovered recently in mouse retina[11, 72] and likely correspond to the OFF-x bipolar cells
232 identified by transcriptomics of human fovea[13] that show an expression profile similar to that of
233 the midget bipolar cells. While most of these cells stratified in the outer half of the IPL (outer-x
234 cells, n = 15, Extended Data Fig. 6a-6b), five of the cells stratified in the inner half of the IPL
235 (inner-x cells, Extended Data Fig. 6c-6g). Another previously undescribed bipolar type showed
236 the characteristic diffuse bipolar cell connection to multiple cones but extended axonal
237 branches in both outer and inner IPL where it provided synaptic output to OFF-outer and ON-
238 inner ganglion cell types (see also Extended Data Fig. 7c, 7e). We refer to this cell group as
239 DBbroad (18 cells, Fig. 3a; Extended Data Fig. 7; Supplementary Data Table 1f). The HFseg1
240 volume offers a unique opportunity to further understand these novel bipolar cell populations.

241 For the amacrine cells the AII type (AC2) was present at the highest density of any amacrine
242 cell population (26%, 75 cells, Figs. 4a, 4b, 5, Supplementary Data Table 1g). This cell type
243 was recognized by its well-established morphology across species[55] including human[40, 56, 73]. A

244 major function of AII cells is to transfer signals from rod bipolar to cone bipolar cells, serving as
245 conduits for rod signals to ganglion cells at scotopic light levels[74]. The presence of AII
246 amacrine cells at such a high density in the fovea, where rods are all but absent, suggests
247 however a function switch to a primary role in photopic spatial vision. Indeed, we observed that
248 AII cells in HFseg1 are postsynaptic to varied cone bipolar types, including IMB cells (Fig. 5).
249 These data support the general view that AII cells "have a day job"[56] to provide an inhibitory
250 pathway from ON to OFF bipolar cells under photopic conditions[74-76] while at the same time
251 emphasizing a specialized synaptic role for the AII cells in the human foveal midget circuit.

252 **Visual pathway reduction: the vertical excitatory connectome**

253 Despite its fundamental nature the number and synaptic architecture of the visual pathways
254 that link the human fovea to the brain is unknown. Our provisional classification of 11 pathways
255 suggests that multiple ganglion cell types (n > 20)[32, 33, 40, 77, 78] observed in the monkey and
256 human retinal periphery are absent from HFseg1. This result also stands in sharp contrast to
257 the retina of the mouse where ~40 GC types have been distinguished throughout the retina[29-31].
258 Our classification however had not to this point ruled out the possibility that some ganglion cell
259 types with somas outside HFSeg1 have dendritic trees which penetrate the volume and
260 contribute to the circuits of the inner retina. We therefore took a second approach to identifying
261 the visual pathways in HFseg1 by mapping what we called the "vertical excitatory
262 connectome".

263 We reasoned, as others have[79], that to generate parallel pathways to the brain each cone
264 photoreceptor must be locally presynaptic to each cone bipolar type (for the S cone, there is
265 uncertainty on this point, due to its more specialized role in color vision). At the next synaptic
266 step, the output of all bipolar cell types should project to all ganglion cell types. In other words,
267 in principle, *all visual pathways should be synaptically linked to the output of any given cone*.

268 To test this hypothesis, we annotated the ribbons within five cones (three LM and two S) and
269 all postsynaptic bipolar cells associated with these cones. For each bipolar cell all synaptic
270 ribbons and their postsynaptic GC partners were next identified (Fig. 8a-8b). Finally, we
271 determined the relative synaptic density from a given cone via its postsynaptic bipolar cells to
272 each identified GC type (see details in Extended Data Figs. 9 and 10; Supplementary Data
273 Table 2).

274 We found that bipolar cells connected to the three LM cones synapsed overwhelmingly with
275 midget and/or parasol ganglion cells (Extended Data Fig. 9), accounting for 92.1% of the total
276 bipolar synaptic output to ganglion cells (Fig. 8c, 8d; Extended Data Fig. 9; Supplementary
277 Data Table 2a-2c). The remaining 7.9% of bipolar synapses were directed to the large field
278 ganglion cell types (LFGC1 - LFGC5, Fig. 7d, 7h, and 7i-7n; Extended Data Fig. 9;
279 Supplementary Data Table 2a-2c). Thus, synaptic density corresponds well with overall cell
280 abundance. Output to dendritic fragments of unidentified ganglion cells was rare, accounting
281 for only ~0.5% of the total bipolar output to ganglion cells (n = 3 LM cones; 0.53 ± 0.76, n = 3
282 LM cones, Supplementary Data Table 2a-2c). These data align with our population analysis
283 described above and show that, for the LM cones, diverse synaptic outputs are overwhelmingly
284 targeted to the midget and parasol pathways.

285

286 **Discussion**

287 **A human foveal connectome.** Our aim was to enable timely completion of a nanometer-scale
288 connectome in the human CNS. Compared to ongoing study of a larger volume of human
289 neocortex[19] our foveal volume has the advantage that foveal circuitry is miniaturized and
290 functionally complete – from receptors to ganglion cell outputs. Moreover, all cell types in the
291 HFSeg1 volume are identified and can be related to anatomical, physiological and
292 transcriptomic studies of human and non-human primate retina (Supplementary Data Table 1).

293 **Cell type profiling.** Datasets parallel to HFseg1 exist for primate central retina where cell
294 types were clustered by gene expression profile and linked to known anatomical types by
295 marker genes[12, 13, 15, 42, 80]. The HFseg1 volume permits a comparison of the two approaches
296 and suggests generally good correspondence though with some unexpected differences. For
297 example, the ratio of H1 to H2 horizontal cell types identified by transcriptomics were shown in
298 macaque and human central retina to be ~3:1 and 7:1 respectively. By contrast the H1 to H2
299 ratio in HFseg1 is much higher (22:1) with H1 cells forming 96% of the horizontal cells at this
300 foveal location. Thus, the trend towards H1 cell dominance in the transcriptomics dataset is
301 evident but more extreme in HFseg1. A similar trend holds for other clearly identified types: for
302 example midget ganglion cells make up ~90% of the ganglion cell population in our sample and
303 86% in the transcriptome; AII cells make up 26% the amacrine cells and 18% of the amacrines
304 identified by transcriptomics. One explanation for the residual differences may be that our
305 smaller sample represents the cone-enriched foveal center whereas the samples used for
306 transcriptomics encompassed a much larger area (~1.5 mm, central 5 degrees). Cell type-
307 specific density changes are extremely steep across this region so that larger spatial samples
308 would average out such changes,

309 Certain cell populations previously recognized were not evident in HFseg1. For example, the
310 recent functional, anatomical and molecular distinction made between diffuse bipolar types

311 DB3a and DB3b in macaque monkey[81, 82] and human retina[13, 83] was not apparent in HFseg1.
312 Further, we found evidence for only 19 amacrine cell types whereas molecular profiling in
313 human retina has proposed 73 amacrine cell types[15]. These differences suggest that the
314 relationship between cells defined by gene expression and anatomical types may not always
315 be straightforward. A further implication is that the extreme increase in density of the midget
316 circuit, required for high acuity and color vision, gives rise to an attendant density increase in
317 other foveal cell types tightly linked to the midget pathway (e.g., H1 horizontal cells) and a
318 decrease in the fovea of cell types concerned with visual processing in the retinal periphery.

319 **The vertical excitatory connectome.** In the retina of the mouse ~40 distinct ganglion cell
320 populations have been recognized[29-31]. In non-human primate fewer than 20 pathways have
321 been defined, with transcriptomic and anatomical identification in reasonable agreement[12, 32, 33].
322 In human fovea, only 12 pathways have been suggested by transcriptomic analysis[13, 15] in near
323 alignment with the current results (see also Supplementary Notes on ganglion cell types). It
324 was nevertheless striking that in the HFseg1 dataset ~96% of the ganglion cells comprised just
325 three anatomically distinct groups: the midget, parasol and small bistratified cells. When we
326 manually traced the vertical connectome from a single cone to its postsynaptic bipolar cells and
327 in turn to all postsynaptic ganglion cells we obtained a corresponding result. Thus, a
328 fundamental, defining feature of foveal synaptic organization may be a reduction in the number
329 of visual pathways compared to peripheral retina. A simple explanation might be the need for
330 the midget circuit to transmit a high-fidelity signal with close to single-cone resolution, meaning
331 that other visual pathways are not required. But there are other major changes in the
332 connectome related to foveal function that remain to be understood. For example, rod
333 photoreceptors are absent or greatly reduced at the foveal center, but how this might impact
334 overall visual pathway cell type diversity and function is unknown. Similarly, the number of

direction-selective visual pathways present in non-primate mammals appears greatly reduced in non-human primates[33, 84] but the significance of this difference remains to be clarified.

The foveal connectome and human color vision.

Most psychophysically-based models of human color vision assume the presence of two parallel color opponent channels: red vs green and blue vs yellow[109]. The red-green pathway shows opposing L vs M cone interaction and has been associated with the circuitry that feeds the midget ganglion cell[85]. However, the human psychophysically defined red-green pathway requires that a small S cone input also be incorporated[86]. The locus of this critical signal pathway remains unclear with recent data from macaque monkey implicating both retina[110] and primary visual cortex[111]. The HFseg1 connectome shows that H1 horizontal cells, a major source of the surround in the midget circuit[51], likely contribute antagonistic signals from all three (L, M and S) cone types, to the midget pathway, thereby offering a novel explanation for an S cone contribution to the human red-green channel. An interaction site early in S, L and M cone pathways of the human fovea is also present in unexpected S-LM cone coupling, which may work to preserve a small, high-fidelity S-cone signal in downstream pathways utilized for trichromatic color vision[87, 88]. Thus, while there is much to learn, HFseg1 already indicates that the connectome will be one route by which we come to understand the unique character of the human nervous system.

Acknowledgements

This work was supported by NIH grants EY-028282 and RF1-MH129260 to D.M.D. and NIH grant P51 OD010425 to the Washington National Primate Research Center and EY01730 to the Vision Research Core at the University of Washington. We thank Sharm Knecht for tissue preparation and managing EM data acquisition.

Author contributions

Y.J.K. and D.M.D. conceived the project. Y.J.K. and D.M.D. generated the ground truth for segmentation and synapses, performed proofreading and created annotations. Y.J.K. and D.M.D. analyzed the data and generated figures. Y.J.K., D.M.D., P.R.M., and U.G., wrote the paper and consulted on figure development. C.A.C. and R.G.S., edited the paper. A.P. acquired human tissue. D.M.D., Y.J.K., C.A.C. and A.P. acquired funding. Zetta AI performed EM data alignment, segmentation, synapse detection and cone-cone contactome detection and ingested all data into the CAVE infrastructure for proofreading. S.G. developed the NeuroMaps.app website with analysis and collaborative proofreading tools.

Declaration of interests

K.L., N.K., D.I., T.N., R.L., S.P., A.H., J.A.B., J.S. and T.M. declare financial interests in Zetta AI. S.G. is owner of Aware LLC and developed the NeuroMaps.app. The remaining authors declare no competing interests.

Figures and figure legends (8 Figures)

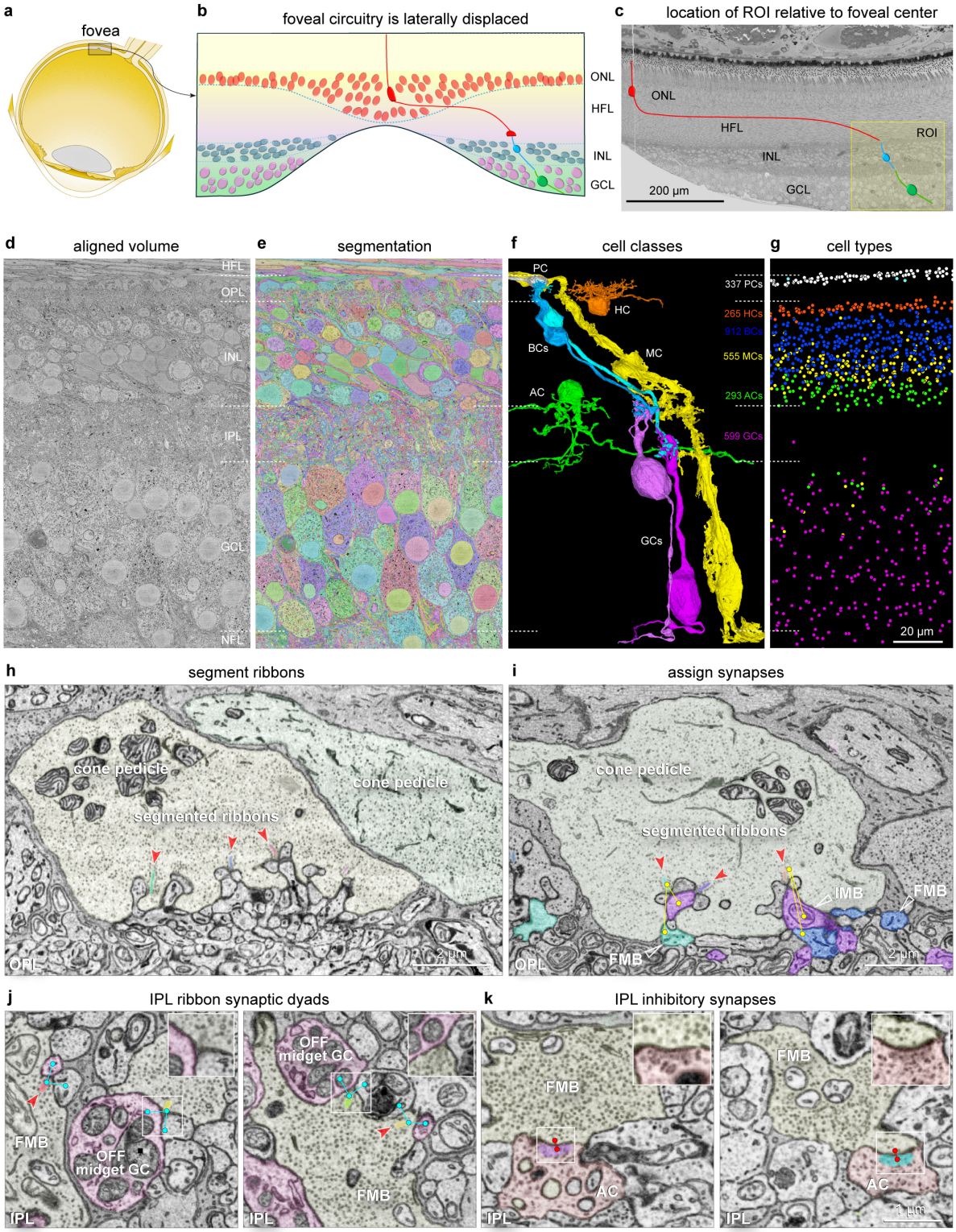

Fig. 1. The HFseg1 volume. **a.** The fovea forms a pit in the retina ~3 mm temporal to the optic disc (within the inset rectangle). **b**. Schematic foveal pit showing cone (red) to bipolar cell (blue) to ganglion cell (green) circuit. ONL, outer nuclear layer, HFL, Henle fiber layer; INL, inner nuclear layer; GCL, ganglion cell layer. **c**. Trimmed retinal block face and ROI (yellow box) in temporal retina 400-500 µm from the foveal center. **d**. Single section from the imaged volume (cropped laterally) to illustrate the retinal layers, HFL, OPL, outer plexiform layer; INL; IPL, inner plexiform layer, GCL and NFL, nerve fiber layer. **e**. Volume segmented into membrane bound objects. **f**. Examples of segmented cells photoreceptor axon terminal (PC, white), horizontal cell (HC, orange), ON and OFF bipolar cells (BC, light and dark blue), Müller glia cell (MC, yellow), amacrine cells (AC, green), ON and OFF ganglion cells (GC, dark and light violet); astrocytes and microglia not shown here. **g**. Numbers and cell soma locations of the cell types shown in **f**. **h.** Three segmented ribbons (varied colors) at synaptic triads (red arrowheads) in a single cone pedicle. **i.** Synaptic assignments associated with each ribbon (yellow dots and lines). An IMB (inner-ON midget bipolar; violet, white open arrowhead) cell makes an invaginating contact and two FMB cells (outer-OFF midget bipolar; light and dark blue, white open arrowheads) make a basal contact with the cone pedicle. **j.** Examples of ribbon and synapse prediction in the inner plexiform layer (IPL) for an FMB cell axon terminal at two locations (left and right panels). Segmented ribbons (varied colors, red arrowheads) and synaptic predictions (blue dots, lines). **k.** Synaptic vesicle cloud segmentation (varied colors) and synaptic prediction (red dots and lines) in the IPL between an amacrine cell and an FMB axon terminal. Insets in **j** and **k** show zoomed view of synapses indicated by white boxes.

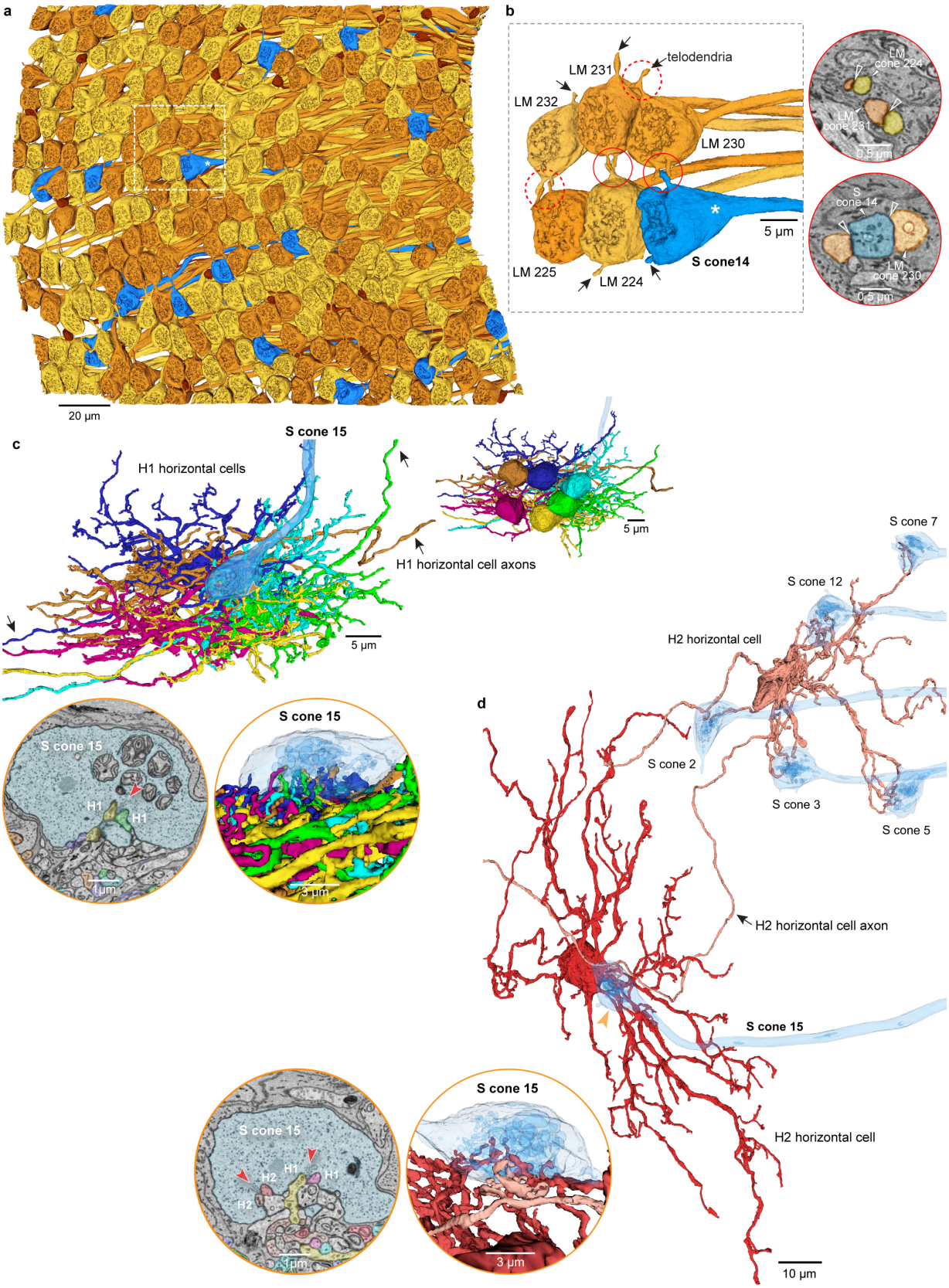
a
20 µm
b
telodendria
LM 231
LM 232
LM 230
LM 225
LM 224
S cone14
5 µm
LM cone 224
LM cone 231
0.5 µm
S cone 14
LM cone 230
0.5 µm
c
S cone 15
H1 horizontal cells
H1 horizontal cell axons
5 µm
5 µm
S cone 15
H1
H1
1 µm
S cone 15
3 µm
d
S cone 7
S cone 12
H2 horizontal cell
S cone 2
S cone 3
S cone 5
H2 horizontal cell axon
S cone 15
H2 horizontal cell
10 µm
S cone 15
H2
H1
H1
H2
1 µm
S cone 15
3 µm

398

399 **Fig. 2. Photoreceptor and horizontal cell populations**. **a**. Array of photoreceptor axon
400 terminals (cone pedicles, rod spherules) viewing the synaptic face of the terminals (297 LM
401 cones, gold; 16 S cones, blue, 24 rods, brown) (see Supplementary Data Table 1a, 1c, 1d). **b**.
402 Six cone pedicles within the white dotted box in **a**. Left, the pedicles contact each other via
403 telodendria (e.g., arrows) within the circled areas. A pedicle identified as an S cone (white
404 asterisk) contacts neighboring LM cone 230. Right, EM micrographs showing telodendritic
405 contacts (open white arrowheads) between LM cones (top) and S cone with LM cone
406 (bottom). **c**. Six overlapping H1 cells are shown (varied colors); each H1 cell forms lateral
407 elements in S cone 15 (blue). Upper inset shows the cell bodies of the six H1 cells. Circle
408 inset at lower left shows EM view of H1 cell lateral elements at a synaptic invagination of S
409 cone 15 (red arrowhead). Circle inset at lower right shows a 3D view of S cone 15 (partial
410 transparency) contacting multiple H1 cells. **d**. Two H2 cells (tan and red) contacting multiple S
411 cones, including S cone 15. Lower insets show H2 cell lateral elements at S cone 15 in single
412 layer EM view (left) and 3D (right) view (conventions as in **c**).

413

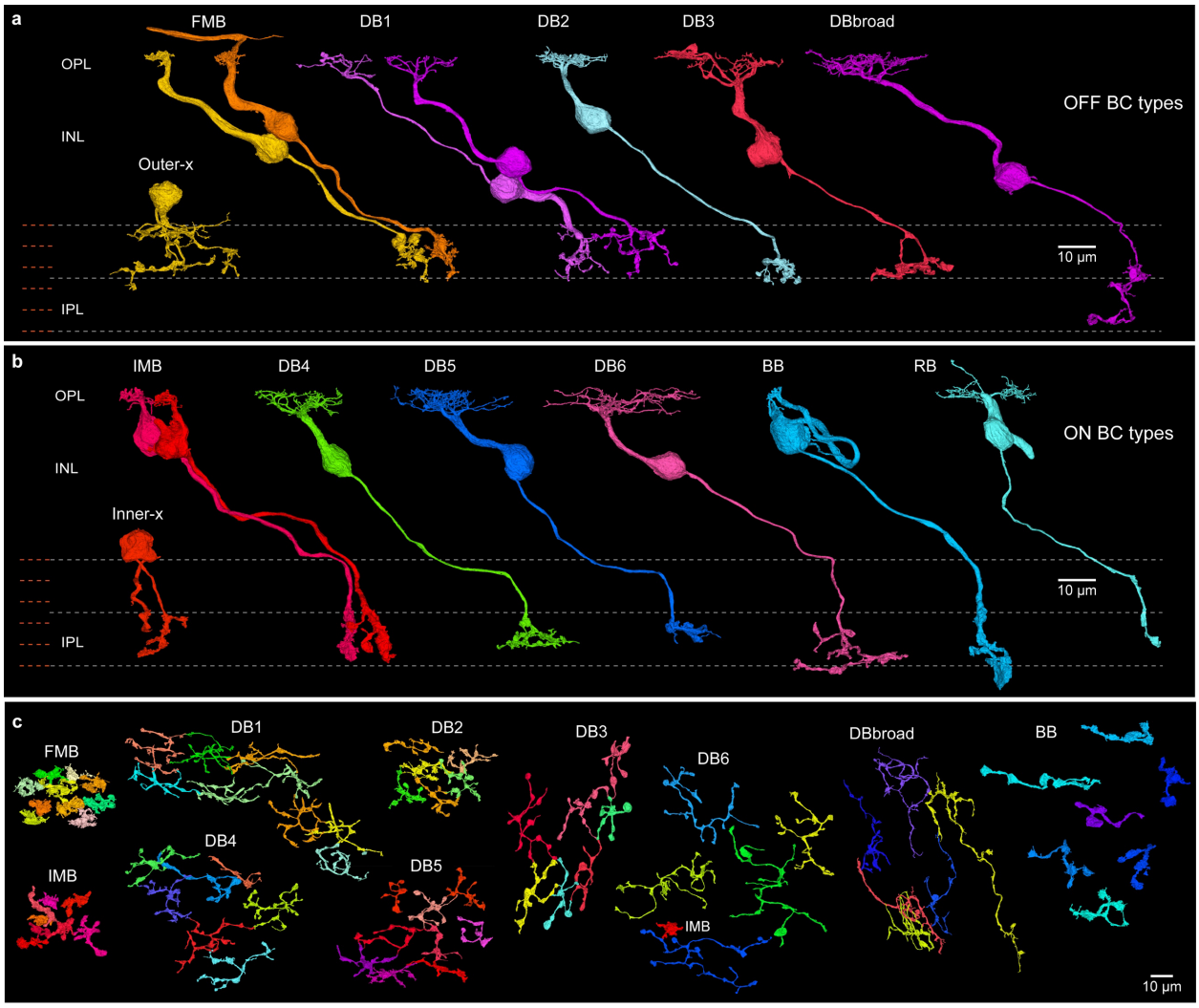

Fig. 3. Bipolar cell types. a. Outer stratifying types (FMB, flat midget bipolar; DB, diffuse bipolar). Outer-x bipolar cells lacked a dendrite but made ribbon synapses in the IPL (Extended Data Fig. 6a). DBbroad cells extend processes across the IPL depth (Extended Data Fig. 7). **b.** Inner stratifying bipolar types; IMB, invaginating midget bipolar; DB, diffuse bipolar types; BB, blue-cone bipolar type, Inner-x bipolar (Extended Data Fig. 6c); RB, rod bipolar. **c**. Horizontal view of spatial mosaics of axon terminals for small groups of neighboring cells of each bipolar type, as indicated.

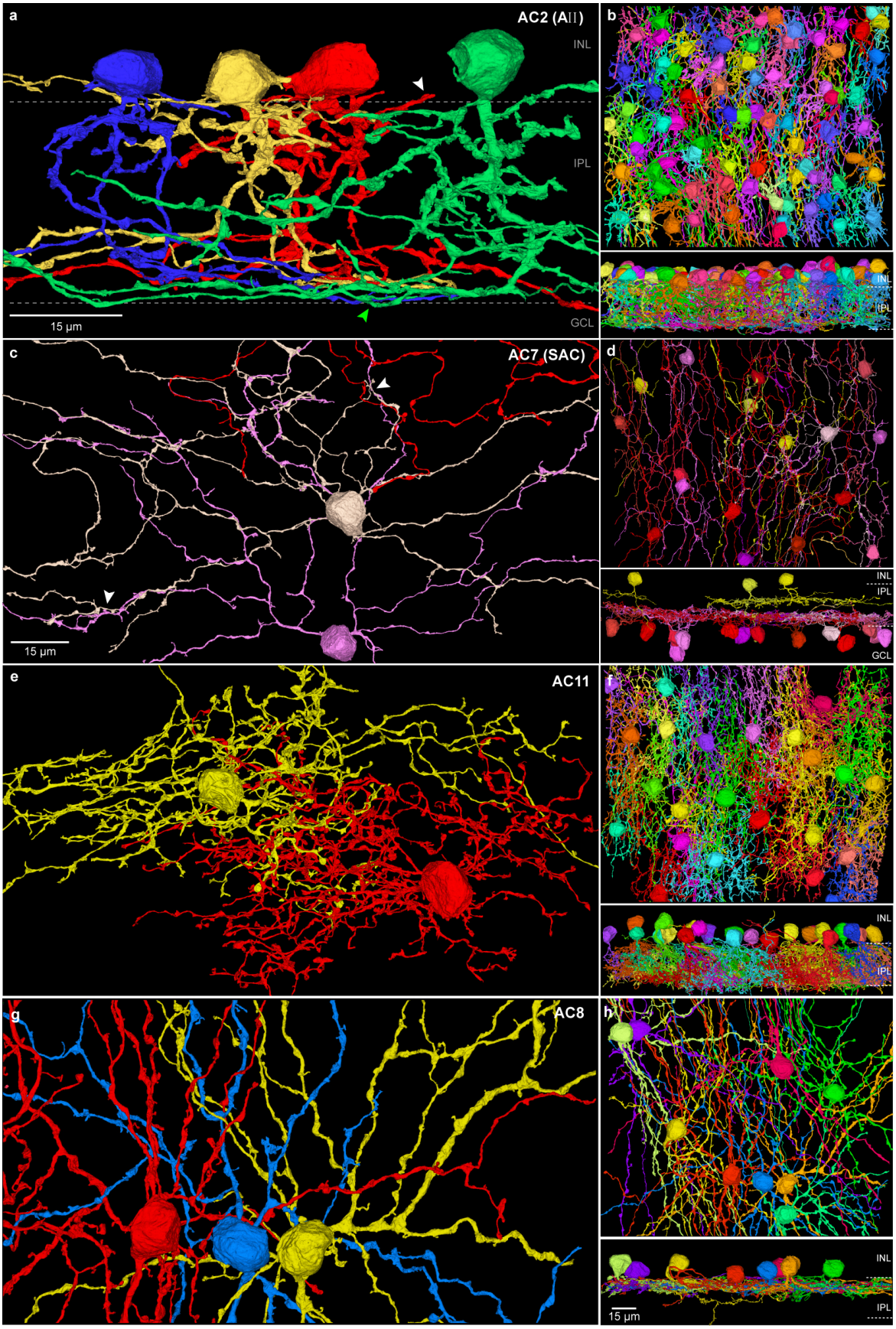
a
AC2 (AII)
INL
IPL
GCL
15 µm
b
INL
IPL
c
AC7 (SAC)
15 µm
d
INL
IPL
GCL
e
AC11
f
INL
IPL
g
AC8
h
INL
IPL
15 µm

423

Fig. 4. Amacrine cells. Amacrine cells in the INL (253 cells) and GCL (40 cells) were divided into 19 types (AC1-19; Supplementary Data Table 1g). **a.** Small field, AII amacrine cells (AC2), in vertical view show outer, lobular dendrites (white arrowhead) and extensive, inner dendrites (green arrowhead). **b.** Horizontal view of the entire AII population in HFseg1; lower panel, vertical view. **c.** Starburst amacrine cells (AC7) were located primarily in the GCL (GCL, 14 cells; INL, 3 cells). White arrowheads indicate typical fasciculation of starburst dendrites. **d.** Mosaic of starburst cells, GCL cells (red-violet) and INL cells (yellow); lower panel, vertical view. **e**. Small field amacrine type (AC11) in horizontal view with densely branched dendritic arbor. **f**. Horizontal view of the AC11 cell mosaic; lower panel, vertical view shows dendrites extend broadly across the IPL. **g.** Large field amacrine cells (AC8) with thick lobular dendrites, narrowly stratified in the outer IPL. **h.** Horizontal view of the complete mosaic; lower panel shows vertical view of outer IPL stratification. Scale bar in **c** applies to **e** and **g**. Scale bar in lower panel of **h** applies to **b, d, f**.

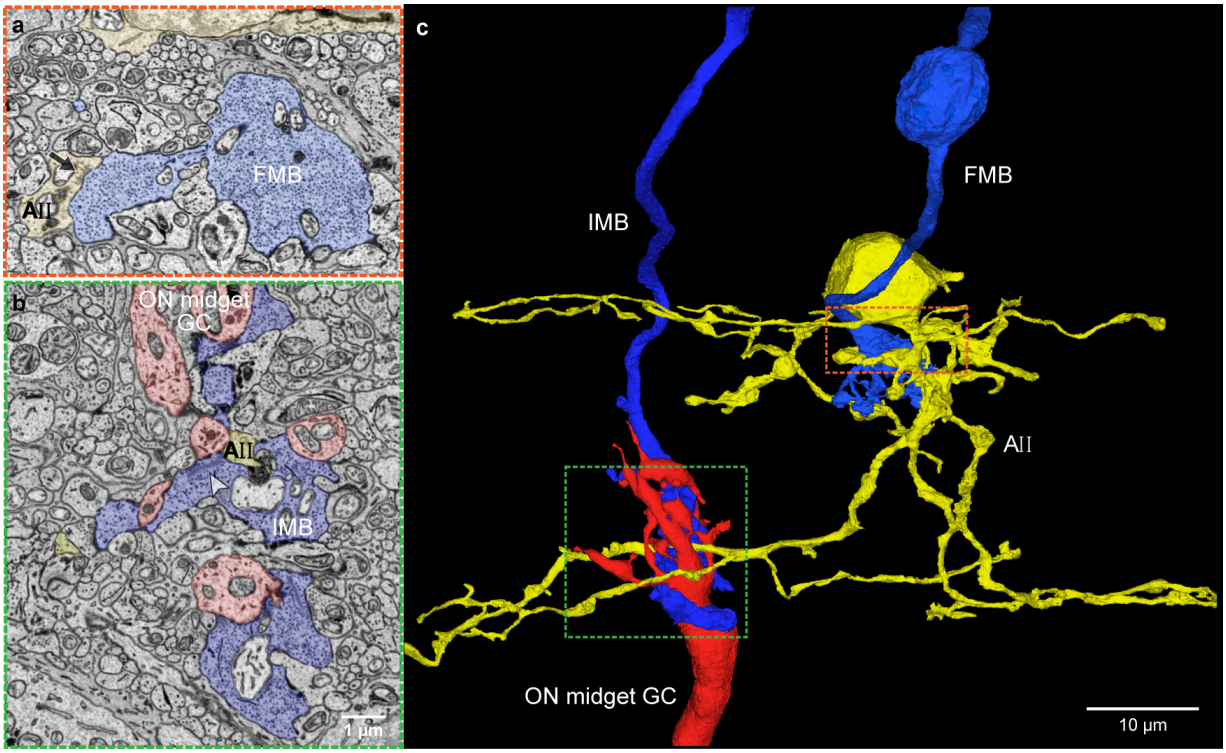

Fig. 5. AII amacrine cells are connected to the ON and OFF midget circuit. **a.** The AII cells provide abundant inhibitory synaptic output to FMB (OFF-midget bipolar) cells (black arrow and orange boxed area in **c**). **b.** Rod bipolar cells are largely absent in HFseg1 volume. This AII cell (yellow) receives alternate excitatory synaptic input from IMB (ON-midget bipolar) cells (white arrowhead and green boxed in **c**). **c.** Vertical 3D view; AII cell shown in yellow. FMB and IMB cells shown in blue. ON midget ganglion cell in red; OFF midget ganglion cell not shown in this image.

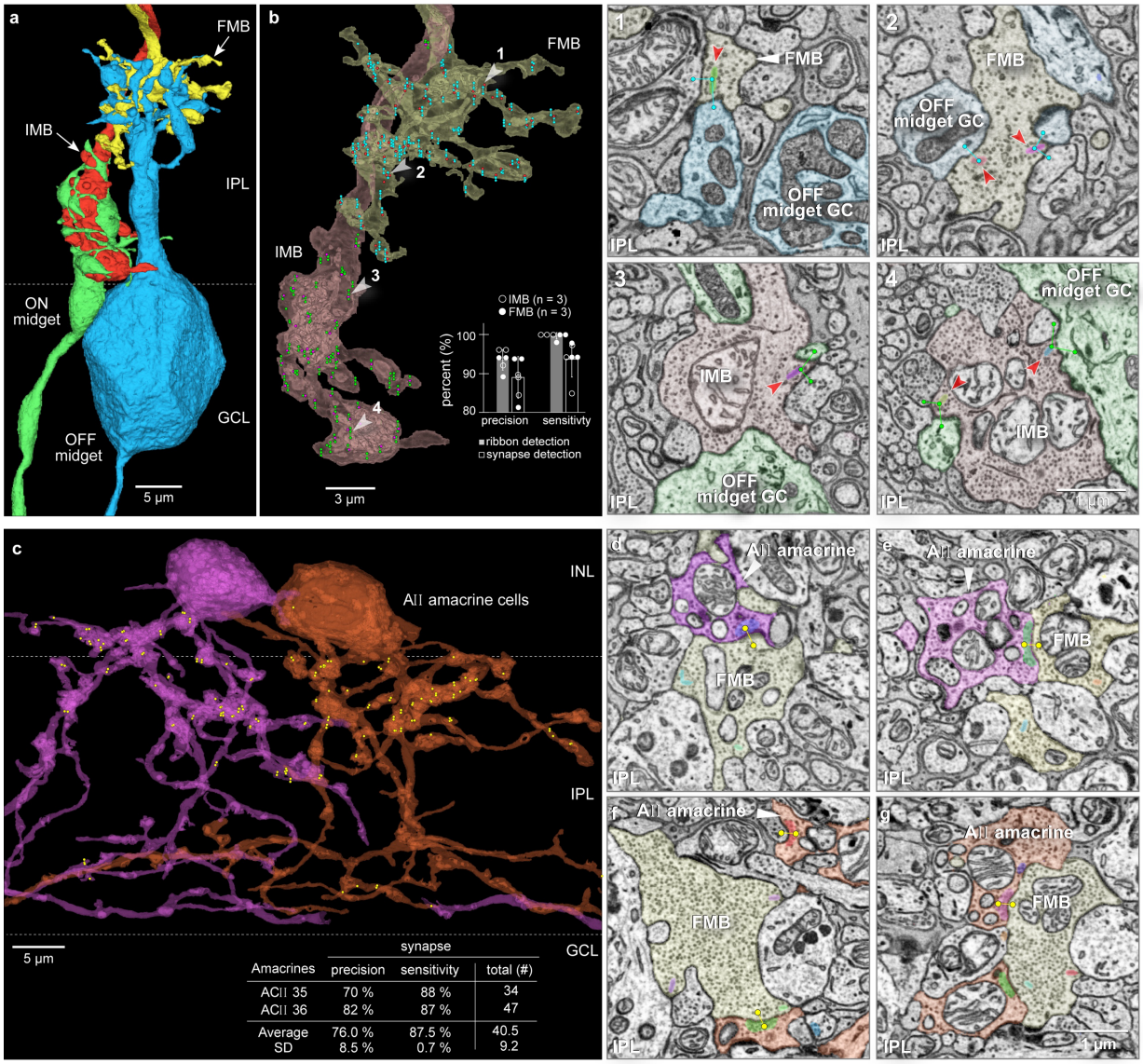

448

449 **Fig. 6. Synapse detection. a**. OFF midget bipolar (yellow) and ON midget bipolar (red)
450 presynaptic to an outer-OFF (blue) and inner-ON (green) midget ganglion cell. **b.** Outgoing
451 synapses detected for the midget bipolar cell axon terminals shown in **a** (ganglion cells
452 removed, semi-transparent view). Synaptic ribbons (red/violet dots) and postsynaptic profiles
453 were first identified manually (see Extended Data Fig. 9; cone 22; BC 308 (IMB) and BC 303
454 (FMB)). Predicted outgoing synapses (green dots and lines, IMB; blue dots and lines, FMB).
455 White arrowheads numbered 1-4 indicate the panels shown on the right in single layer EM

view. Predicted and segmented synaptic ribbons (in varied colors, red arrowheads); predicted postsynaptic segments are marked by the dots and lines linking the synaptic ribbon to its postsynaptic structure (unlabeled postsynaptic profiles belong to amacrine cells). Inset histogram shows precision and sensitivity of ribbon detection and synaptic assignment. **c.** Inhibitory output synapses made by two neighboring AII amacrine cells (purple and orange in partial transparency). Yellow dots show synaptic output predictions; most synaptic outputs arise in the outer half of the IPL and are presynaptic to OFF bipolar cells. Inset shows precision and sensitivity for the synapses made by each AII cell. **d-e**. Single layer images showing segmented vesicle clouds (varied colors) in the purple AII cell (shown in **c**) and synaptic connections predicted with an FMB cell (yellow dots and lines; ribbons in the FMB are also segmented). **f-g**. Same conventions as in **d-e** but showing three segmented vesicle clouds and synaptic predictions for the orange AII cell (shown in **c**), with another FMB cell.

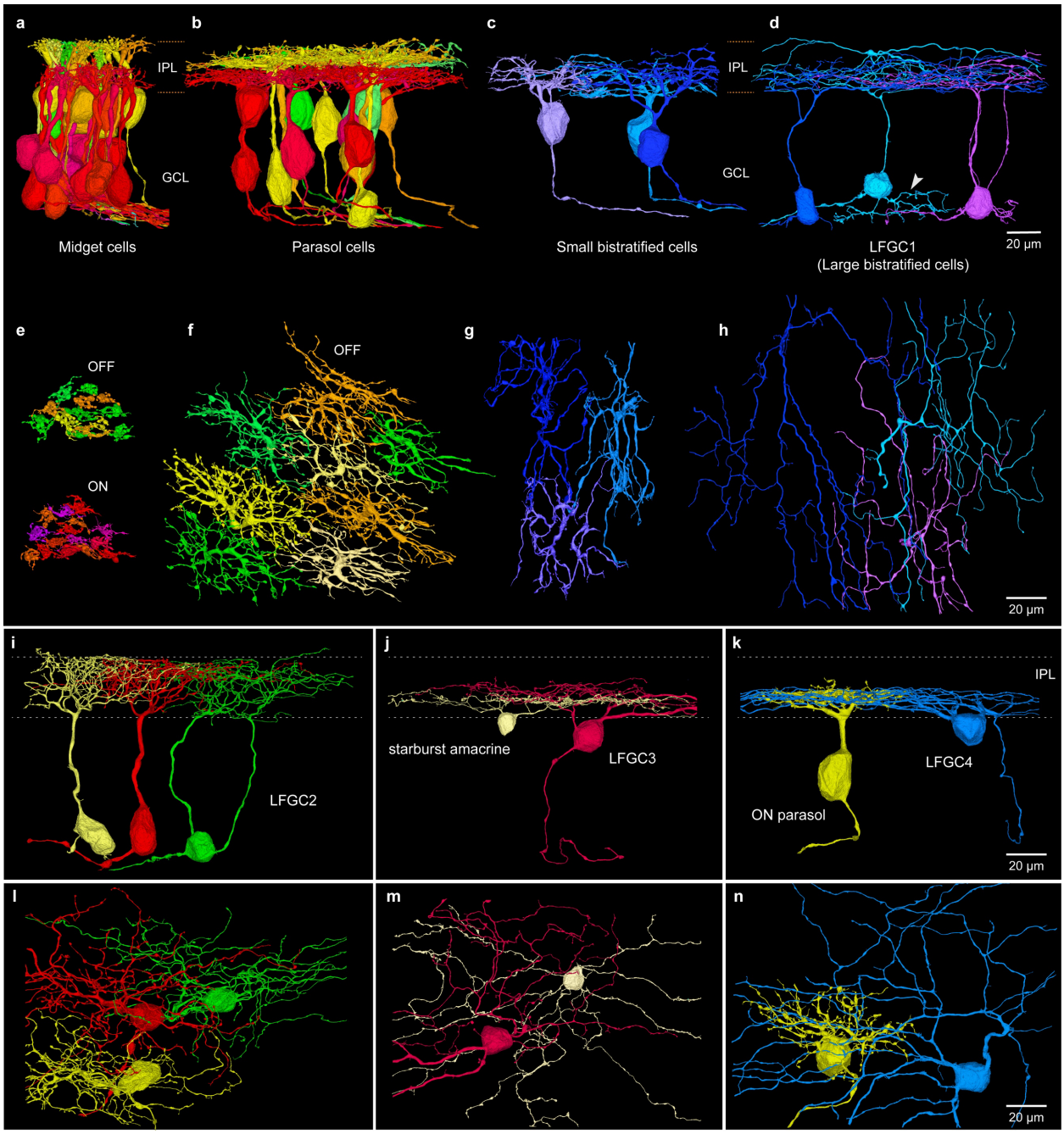

Fig. 7. Ganglion cells. a. Cluster of inner-ON (red-violet) and outer-OFF (yellow-green) midget ganglion cells; dendrites stratify broadly across inner (ON) and outer (OFF) half of the IPL. **b**. Inner-ON (red-violet) and outer-OFF (yellow-green) parasol ganglion cells; dendrites stratify broadly near the center of the IPL. **c**. Small bistratified ganglion cells extend dendrites across the ON-OFF subdivision of the IPL. **d**. Large bistratified ganglion cells (LBGC1) show

large dendritic field and broad stratification. White arrowhead shows branching processes arising from the cell body of unknown significance. **e-h**, Mosaic of dendritic arbors in horizontal view of the same cells shown in **a-d**. **e**. Outer-OFF (yellow-green, top) and inner-ON (red-violet) midget GC. **f**. Outer-OFF parasol cell dendrites show minimal overlap (inner-ON parasol mosaic not shown). **g**. Small bistratified cells show minimal dendritic tree overlap. **h**. LFGC1 (Large bistratified cells) show a much larger and more sparsely branching irregular tree. **i-k**. Morphology of three additional large field types. **i**. LFGC2 (Large diffuse cells) show a densely branched tree broadly stratified across the IPL. **j**. LFGC3 (Recursive bistratified cells) are narrowly bistratified near center of the IPL and tend to fasciculate with starburst amacrine cells. **k**. LFGC4 (Inner smooth monostratified cells) show large, monostratified dendritic trees costratified with parasol cells. **l-n**. Horizontal views of the cells shown in **i-k.**

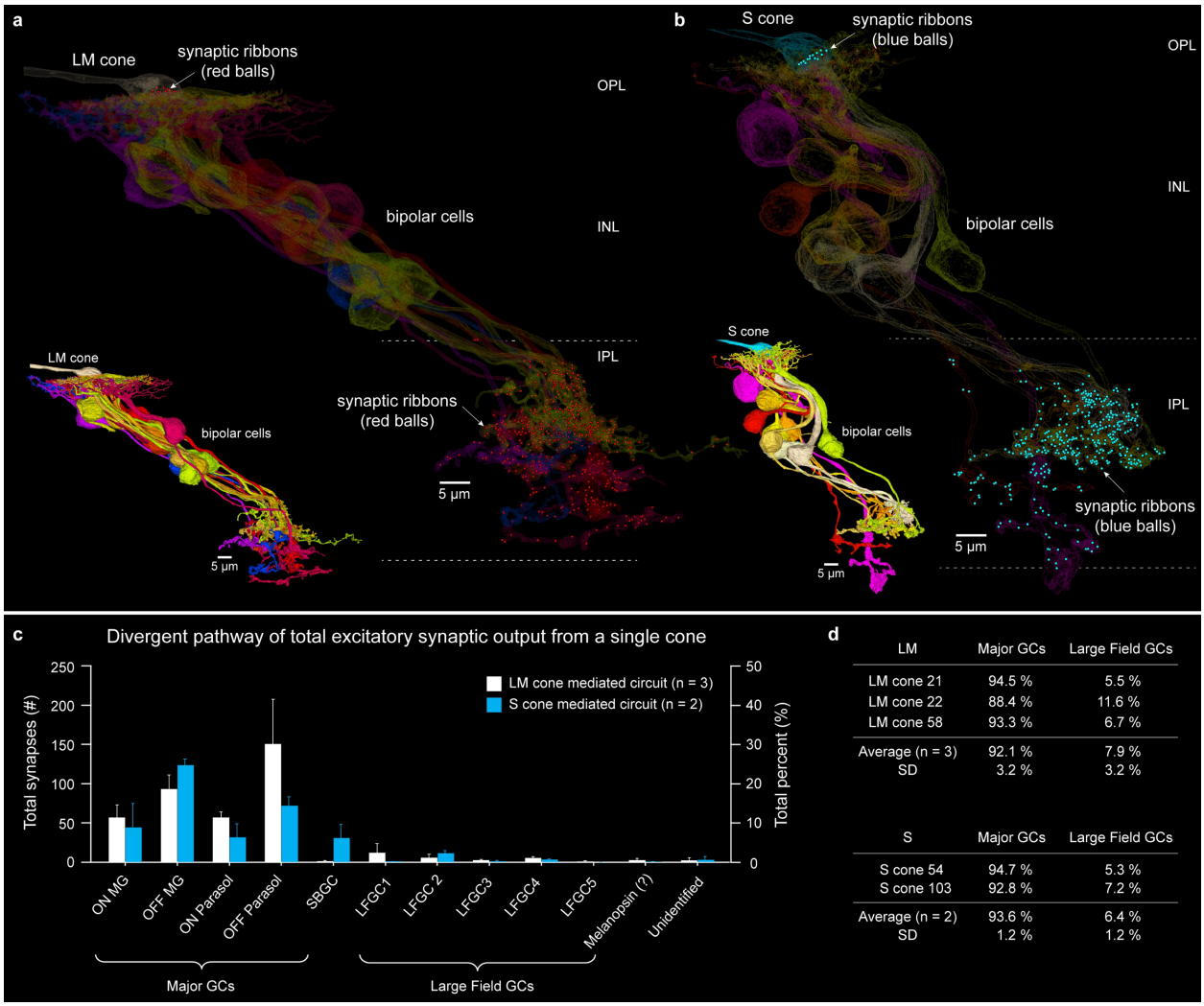

LM	Major GCs	Large Field GCs
LM cone 21	94.5 %	5.5 %
LM cone 22	88.4 %	11.6 %
LM cone 58	93.3 %	6.7 %
Average (n = 3)	92.1 %	7.9 %
SD	3.2 %	3.2 %

S	Major GCs	Large Field GCs
S cone 54	94.7 %	5.3 %
S cone 103	92.8 %	7.2 %
Average (n = 2)	93.6 %	6.4 %
SD	1.2 %	1.2 %

Fig. 8. Vertical excitatory connectome. a. Vertical connectome for a single LM cone (cone 22, see details in Extended Data Fig. 9b). Cone pedicle and postsynaptic bipolar cells shown in silhouette. Synaptic ribbons in the cone pedicle (top, OPL) and bipolar cell axon terminals (lower, IPL) are shown as red balls. Inset shows all bipolar cells postsynaptic to this cone pedicle (outer, yellow-gold; inner, blue-violet-red). **b**. The same views for an identified S-cone (cone 103, see details in Extended Data Fig. 10b; synaptic ribbons, blue dots). **c**. Histogram shows output synapse numbers (left axis), and percent (right axis) made via bipolar cells connected to 3 LM and 2 S cones with postsynaptic GC types. Note that OFF pathway derived synapses greatly outnumber ON pathway synapses. **d**. The great majority of synapses from

LM and S cones are distributed to midget, parasol and small bistratified ganglion cells (Major GCs) with all other large field types receiving 7.9% (LM) and 6.4% (S) of the synaptic output (see also Supplementary Data Table 2). Unidentified processes account for 0.5% of total synaptic output (LM) (see Supplementary Data Table 2a-2c).

504 **Methods**

505 **EXPERIMENTAL MODEL AND SUBJECT DETAILS**

506 **Human tissue acquisition and preparation**

507 Human eyes (52-year-old, white male; brain dead organ donor) were acquired from the
508 Medical University of Vienna, Vienna, Austria at the time of death by surgical enucleation. A
509 small incision was made to give fixative access to the posterior chamber and the retina was in
510 this way immersion fixed in 4% glutaraldehyde in 0.1 M sodium cacodylate buffer, pH7.3-7.4 at
511 room temperature. Medical history confirmed no abnormalities of the visual system recorded
512 and no driving limitations; the ocular status was defined medically as unremarkable at time of
513 enucleation. Eyes were shipped in fixative to the University of Washington where the retinas
514 were dissected and prepared for electron microscopy.

515

516 **METHOD DETAILS**

517 **Identification of foveal ROI, serial block-face SEM sample preparation and image**
518 **acquisition**

519 Retinal tissue was dissected under a dissecting microscope to facilitate identification of the
520 optic disc and the center of the foveal pit as well as the major retinal meridians. We selected
521 an ROI that extends across absolute eccentricity of ~450-650 microns (temporal retina). This
522 location is linked to cones located ~100-300 microns from the foveal pit center due to the
523 lateral migration of retinal circuits from the cones at the foveal center. This location
524 encompasses much of the central 1 degree (~300 μm/deg) of visual angle (Fig. 1a-1c).

525 The dissected retina was then plastic embedded and prepared for electron microscopy as
526 previously described[1]. In brief, the tissue was incubated in a 1.5% potassium ferrocyanide and
527 2% osmium tetroxide (OsO4) solution for 1 h. After washing, the tissue was placed in a freshly

528 made thiocarbohydrazide solution for 20 min and then rinsed and incubated in 2% OsO4 for
529 30 min. Lastly, the tissue was stained en bloc in 1% uranyl acetate overnight and
530 subsequently stained with Walton's lead aspartate, dehydrated and plastic embedded
531 (Durcupan, 44610, Sigma Aldrich). After evaluation of the ROI by semithin sectioning the
532 tissue block was trimmed, gold-coated by standard methods, and mounted in an Apreo SEM
533 Volumescope (Thermo Fisher). We cut 3028 sections at 50 nm thick for a total depth of ~150
534 microns, imaging an ROI (180 μm tall x 180 μm wide; 5 nm pixels) that encompassed the full
535 vertical depth of the retina, from the Henle fiber layer (HFL) to the nerve fiber layer (Fig. 1d).
536 The overall ROI was imaged on the blockface after each section as 25 sequential tiles (8000 x
537 8000 pixels or 40 x 40 μm; 75,700 total image tiles) with 10% overlap. Images were stitched
538 within layer and aligned across layers using standard methods available in TrakEM2 [2] (NIH
539 image plugin; Scale Invariant Feature Transform (SIFT) with affine translation) to create a
540 good quality volume. We first evaluated this TrakEM2-aligned volume by manual
541 reconstruction of a small number of selected cells and circuits [62]. To further develop this
542 volume as a connectomic resource we applied deep-learning based computational
543 approaches to realign, segment and reconstruct all cells and synaptic connections as follows
544 [22, 38].

545 **Volume creation**

546 *Montaging.* Tile offsets were determined manually, then refined by template matching at 40 nm
547 with a search window of 96 pixels. Tiles were cropped by 128 pixels to avoid edge distortions
548 and placed to minimize the sum of least squares from the new offsets. Outliers were inspected
549 and given manual placement. These cropped tiles were processed to create a pyramid of
550 encodings for resolutions between 20 nm and 640 nm [89], and then stitched to make the
551 montaged section in two steps. In the first step, only the two neighboring tiles in Y were
552 considered, with both neighbors being fixed. Using an online finetuner pyramid [89] with the

553 calculated placement as the starting point, a displacement field was generated that would
554 warp the encoded tiles to minimize the pixel difference with the fixed tiles. The encoded tiles
555 were then warped using this displacement field, eroded by a pixel to avoid partial pixels at the
556 edge, blended to the fixed tiles using the mean of the pixel values in the overlap, and then
557 passed through CLAHE enhancement to mitigate the contrast loss from the warping and
558 blending, resulting in strips of encoded tiles where every other tile had been warped. In the
559 second step, the strips of tiles from the first step were stitched to each other, holding every
560 other strip fixed in a similar process. An error map was generated at both steps by computing
561 the difference between the encodings in the overlap at 40 nm and inspected. The non-
562 encoded tiles were cropped by 394 pixels, warped according to the composed displacement
563 fields from the encodings, and combined to yield montaged sections.

564 *Alignment.* The unaligned sections were first processed to create a pyramid of encodings [89]. A
565 rigid transformation for the entire dataset was estimated using SIFT features [90] extracted from
566 the encodings at 640 nm and correspondences established between nearest and next-nearest
567 section pairs. From the rigidly aligned encodings, displacement fields at 40 nm resolution were
568 generated between nearest and next-nearest section pairs using an online finetuner pyramid [89].

569 A convolutional net trained to detect local misalignments and/or simple mismatches caused by
570 defects in the EM images was used to mask unreliable regions in each displacement field. In
571 addition, 25 sections with defects that presented with non-smooth deformations were masked
572 by hand. Pairwise displacement fields and transformation masks were then passed to a global
573 relaxation [89, 91]. This relaxation was performed first at 2560 nm across all 3028 sections of the
574 dataset, and subsequently in blocks of approximately 100 sections at a resolution of 640 nm,
575 using the previously generated drift-free fields as constraints for the start and end sections of
576 each of the 31 blocks. The resulting displacement fields were composed with the earlier rigid
577 transformation and the final aligned image stack warped and rendered at 10 nm.

578 *Segmentation.* We pretrained a convolutional net to predict affinities between neighboring
579 voxels at 16×16×40 nm³ using 1,368 μm³ of manually annotated data derived from three
580 mouse visual cortex datasets [92]. We used the residual symmetric U-Net architecture [93] with
581 modifications [94] and trained with data augmentation previously described [95]. We trained the
582 network for 2,000,000 iterations using four NVIDIA L4 GPUs with PyTorch data parallelism,
583 where each GPU processed individual patches with its own model replica.

584 To further fine-tune this network, we manually created training data consisting of 39 μm³ at a
585 resolution of 20×20×50 nm³. In contrast to the pretraining datasets, mitochondria were
586 intentionally over segmented to bias boundary detection toward a more conservative
587 approach, aiming primarily to reduce merge errors at the expense of increasing split errors.
588 Although we initially hypothesized that this mitochondrial over segmentation would minimally
589 impact neuron reconstruction accuracy, we observed that it occasionally resulted in split errors
590 in scenarios where mitochondria were tightly enclosed within very thin neuronal branches.
591 Nevertheless, due to the substantial reduction in merge errors achieved by this strategy, we
592 considered the corresponding increase in split errors acceptable. The training setup for fine-
593 tuning was identical to the pretraining configuration. We fine-tuned the network for 300,000
594 iterations.

595 We predicted an affinity map for the whole dataset. Dark voxels could sometimes span
596 multiple cells and cause segmentation errors. We therefore applied a binarized mask for dark
597 voxels with a threshold of 0.2, invalidating each dark voxel and its three incident affinities. The
598 resulting masked affinity map was then segmented with a mean affinity agglomeration
599 threshold of 0.25 [95]. The segmentation was ingested into the Connectome Annotation
600 Versioning Engine proofreading platform, CAVE[96] for further analysis.

601 CAVE permitted proofreading to be performed by a user community accessing the web-based
602 neuroglancer interface [95, 97] with dynamic updating of segment ID and related synaptic

603 connectivity. We named this segmented volume HFseg1 (Human Fovea, segmentation 1).
604 The HFseg 1 segmentation was of high initial quality such that it was possible to identify and
605 annotate all major cell classes within the volume and to sort these cells into populations of
606 distinct types using the annotation tools available in neuroglancer. Current annotations have
607 been ingested into CAVE and provide a cell type ID hypothesis that can later be tested for
608 each proposed cell population by further analysis of synaptic connectivity. All cells are
609 accessible at NeuroMaps (https://neuromaps.app).

610 Cell types were identified provisionally based on segment 3D morphology (dendritic
611 morphology, stratification depth, and spatial regularity and interaction (mosaics) and in some
612 cases nuclear morphology) with proofreading ongoing (> 25,000 edits) and applied thus far to
613 correct larger obvious mergers (primarily with glial cell processes) that interfered with cell type
614 identification and additional more detailed proofreading on circuits of interest in the current
615 survey of cone-bipolar-ganglion cell connections. The majority of cell populations were
616 unambiguously recognized based on previous studies of primate retina [40, 98, 99] (e.g., the S
617 cones, the H1 and H2 horizontal cells, the starburst and AII amacrine cell types, the midget,
618 diffuse and blue-cone bipolar types, or the midget, parasol and small bistratified ganglion cell
619 types); some cell types (mainly low density amacrine types) were provisionally designated
620 subject to further proofreading and connectivity analysis. The properties and relative densities
621 of these cell types provide the starting point from which the full synaptic connectome can be
622 determined after proofreading by the community, and the assignment of synaptic connections
623 to each cell in the volume. Following FlyWire[39], we have initiated an open community of retinal
624 neurobiologists (currently 7 labs participating) to use these tools to complete proofreading of
625 the HFseg1 volume.

626 **Synapse detection**

627 *Ribbon synapse detection in OPL and IPL.* A symmetric residual U-Net architecture was
628 trained on data with a resolution of 10×10×50 nm^3 using input patches of size 128×128×20 to
629 generate a probability map that indicates the likelihood of each voxel belonging to a synaptic
630 ribbon [100]. To remove less robust predictions at the boundaries, only the central 96×96×16
631 voxels of the input patch was used as the output. The model was trained on a total volume of
632 2,254 μm^3 of manually labeled cutouts sampled from various regions across the entire
633 dataset.

634 The ribbon segmentation was produced by (1) down sampling the probability map by 2×, (2)
635 thresholding for voxels above 0.15, and (3) using 26-connectivity to extract connected
636 components. Segments smaller than 5 voxels in a 20×20×50 nm^3 resolution were neglected to
637 eliminate spurious detections.

638 To achieve ribbon detection in the OPL segments smaller than 5 voxels in a 20×20×50 nm^3
639 resolution within the bounds of the OPL were neglected to eliminate spurious detections. For
640 each detected ribbon within a cone pedicle, postsynaptic partners were automatically
641 identified via the following steps: (1) All neighboring segments touching the pedicle within 800
642 nm of the ribbon centroid were identified. (2) For each neighbor, a representative point close
643 to the ribbon was chosen as the postsynaptic site. These constitute the set of putative
644 synapses for each ribbon. (3) After cell identification, only putative synapses onto bipolar or
645 horizontal cells were kept; all others were filtered out (e.g. Müller glia, neighboring cones,
646 mitochondria). (4) Finally, for each distinct ribbon-postsynaptic cell pair, all but the shortest
647 putative synapses were filtered out. The result was that for each ribbon in a cone, a single
648 synaptic connection was found onto any bipolar or horizontal cell making contact with that
649 cone pedicle within 800 nm.

650 For synaptic ribbons in the IPL segments smaller than 50 voxels in a 20×20×50 nm^3 resolution
651 within the bounds of the IPL were neglected to eliminate spurious detections. For each

652 detected ribbon, postsynaptic partners were automatically identified via the following steps: (1)
653 Identify the two largest profiles within a small (500 nm) window of the centroid of the ribbon
654 which are adjacent to the presynaptic cell and are also adjacent to each other. (2) If such a
655 pair is found, the ribbon is assumed to be presynaptic to both (i.e., a dyadic synapse). (3) If no
656 such pair is found, then within the window, the single largest profile adjacent to the
657 presynaptic cell is identified as the postsynaptic partner. (4) Putative synaptic connections
658 were filtered by cell type, requiring the presynaptic cell to be previously annotated as a bipolar
659 cell, and the postsynaptic partner to be previously annotated as amacrine, or ganglion cell.
660 Note we did not at this time try to use a convolutional net to detect a low density of possibly
661 ribbonless synapses.

662 *Vesicle cloud detection and conventional synapse assignment in the IPL.* A symmetric residual
663 U-Net architecture was trained on data with a resolution of 10×10×50 nm^3 using input patches
664 of size 128×128×20 to generate a probability map that indicates the likelihood of each voxel
665 belonging to a vesicle cloud [100]. To remove less robust predictions at the boundaries, only the
666 central 96×96×16 voxels of the input patch was used as the output. The model was trained on
667 a total volume of 2,254 μm^3 of manually labeled cutouts sampled from various regions across
668 the entire dataset (the same cutouts as ribbon synapse detection). Manual labels were
669 roughly annotated to mark approximate locations of vesicle clouds rather than precise
670 boundaries.

671 The vesicle cloud segmentation was produced by (1) downsampling the probability map by
672 2×, (2) thresholding for voxels above 0.15, and (3) using 26-connectivity to extract connected
673 components. Segments with fewer than 200 voxels were excluded, based on the range of
674 vesicle cloud sizes encountered.

675 *IPL conventional synapse assignment*. A symmetric residual U-Net architecture was trained on
676 data with a resolution of 20×20×50 nm^3 using input patches of size 24×24×8 to generate a
677 probability map that indicates the likelihood of each voxel belonging to the postsynaptic cell
678 [100]. The model was trained on 682 μm^3 of manually annotated labeled cutouts.

679 The model was applied once for each vesicle cloud detected, in a window centered on the
680 centroid of the vesicle cloud. Using the initial automatic cell segmentation, the cell with the
681 highest mean probability within the window was selected as the putative postsynaptic partner
682 [100]. Further filtering by cell type was applied, requiring the presynaptic cell to be previously
683 annotated as an amacrine cell, and the postsynaptic partner to be previously annotated as
684 amacrine, bipolar, or ganglion cell.

685 *Generating the cone-cone contactome.* We identified gap junctions between cone pedicles
686 and between cone pedicles and rods as follows. Cones and rods were manually identified and
687 proofread to completion. Contacts were computed using abiss [101] where a contact is
688 considered to be a set of connected voxel faces that are shared by the same pair of
689 segments. For each contact, we counted the number of voxel faces along each orientation (xy,
690 xz, and yz), as well as the minimum bounding box containing all of the faces. The surface area
691 of a contact was estimated by computing the sum of the area of all faces involved. Contacts
692 were excluded from analysis if (1) the surface area of the contact was $\leq$0.04 μm^2 (mean
693 surface area of contact, 0.55 ± 0.3 μm^2, n = 1141 cone-cone contacts) or (2) the center of the
694 bounding box was more than 15 μm from the approximate center of the cone pedicle
695 (manually identified). All remaining contacts were manually inspected with 1× coverage to
696 determine if they corresponded to what would be manually identified as a true cone-cone
697 contacts harboring gap junctions.

698 **Proofreading, synaptic connectivity and updating with the Connectome Annotation**
699 **Versioning Engine (CAVE)**

As noted above we ingested synapse predictions and cell type annotations into CAVE. A critical functionality given by CAVE is that is allows collaborative users to programmatically query the up-to-date proofread connectivity graph (synaptic connectivity is updated during proofreading of each segment-cell type) as well as any changes made to the metadata (cell type IDs, descriptions, or other annotations). We used the Jupyter notebook application to execute Python code that queried the HFseg1 dataset by leveraging Python libraries that interact with the human foveal dataset, enabling access to segment IDs and synaptic assignments.

DATA AND SOFTWARE AVAILABILITY

The HFseg1 dataset (volume, segmentation, synaptic detection and full annotation) are currently hosted by Zetta.ai (https://zetta.ai/) and all data is accessible for community proofreading by permission at NeuroMaps. The latest version of the HFseg1 dataset is also available at NeuroMaps (https://neuromaps.app).

716 **References**

717 1. Ramon y Cajal, S. La rètine des vertèbrès. *La Cellule* **9**, 119-257 (1892).

718 2. Masland, R.H. & Raviola, E. Confronting complexity: strategies for understanding the
719 microcircuitry of the retina. *Annual review of neuroscience* **23**, 249-284 (2000).

720 3. Dowling, J.E. *The Retina: An approachable part of the brain* (Harvard University Press,
721 Cambridge, MA, 2012).

722 4. Rodieck, R.W. *The First Steps in Seeing* (Sinauer Associates, Inc., Sunderland MA, 1998).

723 5. Helmstaedter, M.*, et al.* Connectomic reconstruction of the inner plexiform layer in the
724 mouse retina. *Nature* **500**, 168-174 (2013).

725 6. Kim, J.S.*, et al.* Space-time wiring specificity supports direction selectivity in the retina.
726 *Nature* **509**, 331-336 (2014).

727 7. Briggman, K.L., Helmstaedter, M. & Denk, W. Wiring specificity in the direction-selectivity
728 circuit of the retina. *Nature* **471**, 183-188 (2011).

729 8. Anderson, J.R.*, et al.* Exploring the retinal connectome. *Molecular vision* **17**, 355-379
730 (2011).

731 9. Calkins, D.J., Schein, S.J., Tsukamoto, Y. & Sterling, P. M and L cones in macaque fovea
732 connect to midget ganglion cells by different numbers of excitatory synapses. *Nature* **371**,
733 70-72 (1994).

734 10. Calkins, D.J. & Sterling, P. Absence of spectrally specific lateral inputs to midget ganglion
735 cells in primate retina. *Nature* **381**, 613-615 (1996).

736 11. Shekhar, K.*, et al.* Comprehensive Classification of Retinal Bipolar Neurons by Single-Cell
737 Transcriptomics. *Cell* **166**, 1308-1323 e1330 (2016).

12. Peng, Y.R.*, et al.* Molecular Classification and Comparative Taxonomics of Foveal and Peripheral Cells in Primate Retina. *Cell* **176**, 1222-1237 (2019).

13. Yan, W.*, et al.* Cell Atlas of The Human Fovea and Peripheral Retina. *Sci Rep* **10**, 9802 (2020).

14. Hahn, J.*, et al.* Evolution of neuronal cell classes and types in the vertebrate retina. *Nature* **624**, 415-424 (2023).

15. Li, J.*, et al.* Integrated multi-omics single cell atlas of the human retina. *Res Sq* (2023).

16. Dorkenwald, S.*, et al.* Neuronal wiring diagram of an adult brain. *Nature* **634**, 124-138 (2024).

17. Azevedo, A.*, et al.* Connectomic reconstruction of a female Drosophila ventral nerve cord. *Nature* **631**, 360-368 (2024).

18. Abbott, L.F.*, et al.* The Mind of a Mouse. *Cell* **182**, 1372-1376 (2020).

19. Shapson-Coe, A.*, et al.* A petavoxel fragment of human cerebral cortex reconstructed at nanoscale resolution. *Science* **384**, eadk4858 (2024).

20. Loomba, S.*, et al.* Connectomic comparison of mouse and human cortex. *Science* **377**, eabo0924 (2022).

21. Lichtman, J.W. & Sanes, J.R. Ome sweet ome: what can the genome tell us about the connectome? *Current opinion in neurobiology* **18**, 346-353 (2008).

22. Turner, N.L.*, et al.* Reconstruction of neocortex: Organelles, compartments, cells, circuits, and activity. *Cell* **185**, 1082-1100 e1024 (2022).

23. Ding, Z.*, et al.* Functional connectomics reveals general wiring rule in mouse visual cortex. *Nature* **640**, 459-469 (2025).

24. Wandell, B.A., Dumoulin, S.O. & Brewer, A.A. Visual field maps in human cortex. *Neuron* **56**, 366-383 (2007).

25. Sereno, M.I., Sood, M.R. & Huang, R.S. Topological Maps and Brain Computations From Low to High. *Frontiers in systems neuroscience* **16**, 787737 (2022).

26. Harvey, B.M. & Dumoulin, S.O. The relationship between cortical magnification factor and population receptive field size in human visual cortex: constancies in cortical architecture. *J Neurosci* **31**, 13604-13612 (2011).

27. Sereno, M.I.*, et al.* Borders of multiple visual areas in humans revealed by functional magnetic resonance imaging. *Science* **268**, 889-893 (1995).

28. Schira, M.M., Tyler, C.W., Breakspear, M. & Spehar, B. The foveal confluence in human visual cortex. *J Neurosci* **29**, 9050-9058 (2009).

29. Baden, T.*, et al.* The functional diversity of retinal ganglion cells in the mouse. *Nature* **529**, 345-350 (2016).

30. Bae, J.A.*, et al.* Digital Museum of Retinal Ganglion Cells with Dense Anatomy and Physiology. *Cell* **173**, 1293-1306 e1219 (2018).

31. Goetz, J.*, et al.* Unified classification of mouse retinal ganglion cells using function, morphology, and gene expression. *Cell reports* **40**, 111040 (2022).

32. Masri, R.A., Percival, K.A., Koizumi, A., Martin, P.R. & Grünert, U. Survey of retinal ganglion cell morphology in marmoset. *J Comp Neurol* **527**, 236-258 (2019).

33. Kim, Y.J.*, et al.* Origins of direction selectivity in the primate retina. *Nature communications* **13**, 2862 (2022).

34. Curcio, C.A., Sloan, K.R., Kalina, R.E. & Hendrickson, A.E. Human photoreceptor topography. *J.Comp.Neurol.* **292**, 497-523 (1990).

783 35. Curcio, C.A., Kar, D., Owsley, C., Sloan, K.R. & Ach, T. Age-Related Macular
784 Degeneration, a Mathematically Tractable Disease. *Investigative ophthalmology & visual*
785 *science* **65**, 4 (2024).

786 36. Schein, S.J. Anatomy of macaque fovea and spatial densities of neurons in foveal
787 representation. *J Comp Neurol* **269**, 479-505 (1988).

788 37. Drasdo, N., Millican, C.L., Katholi, C.R. & Curcio, C.A. The length of Henle fibers in the
789 human retina and a model of ganglion receptive field density in the visual field. *Vision Res*
790 **47**, 2901-2911 (2007).

791 38. Lee, K.*, et al.* Convolutional nets for reconstructing neural circuits from brain images
792 acquired by serial section electron microscopy. *Current opinion in neurobiology* **55**, 188-
793 198 (2019).

794 39. Dorkenwald, S.*, et al.* FlyWire: online community for whole-brain connectomics. *Nature*
795 *methods* **19**, 119-128 (2022).

796 40. Grünert, U. & Martin, P.R. Cell types and cell circuits in human and non-human primate
797 retina. *Progress in retinal and eye research*, 100844 (2020).

798 41. Grünert, U. & Martin, P.R. Morphology, Molecular Characterization, and Connections of
799 Ganglion Cells in Primate Retina. *Annu Rev Vis Sci* **7**, 73-103 (2021).

800 42. Zhang, L.*, et al.* Evolutionary and developmental specialization of foveal cell types in the
801 marmoset. *Proceedings of the National Academy of Sciences of the United States of*
802 *America* **121**, e2313820121 (2024).

803 43. Kim, Y.J.*, et al.* Comparative connectomics reveals noncanonical wiring for color vision in
804 human foveal retina. *Proceedings of the National Academy of Sciences of the United*
805 *States of America* **120**, e2300545120 (2023).

806 44. Dacey, D.M. The mosaic of midget ganglion cells in the human retina. *J.Neurosci.* **13**,
807 5334-5355 (1993).

808 45. Dacey, D.M. Morphology of a small-field bistratified ganglion cell type in the macaque and
809 human retina. *Visual neuroscience* **10**, 1081-1098 (1993).

810 46. Dacey, D.M. & Lee, B.B. The blue-ON opponent pathway in primate retina originates from
811 a distinct bistratified ganglion cell type. *Nature* **367**, 731-735 (1994).

812 47. Chichilnisky, E.J. & Baylor, D.A. Receptive-field microstructure of blue-yellow ganglion
813 cells in primate retina. *Nat.Neurosci.* **2**, 889-893 (1999).

814 48. Calkins, D.J., Tsukamoto, Y. & Sterling, P. Microcircuitry and mosaic of a blue-yellow
815 ganglion cell in the primate retina. *J.Neurosci.* **18**, 3373-3385 (1998).

816 49. Masri, R.A., Greferath, U., Fletcher, E.L., Martin, P.R. & Grünert, U. Immunohistochemistry
817 and spatial density of Müller cells in the human fovea. *Investigative ophthalmology &*
818 *visual science* **in press** (2025).

819 50. Singaravelu, J., Zhao, L., Fariss, R.N., Nork, T.M. & Wong, W.T. Microglia in the primate
820 macula: specializations in microglial distribution and morphology with retinal position and
821 with aging. *Brain Struct Funct* **222**, 2759-2771 (2017).

822 51. Goyal, M., Bordt, A.S., Neitz, J. & Marshak, D.W. Trogocytosis of neurons and glial cells by
823 microglia in a healthy adult macaque retina. *Sci Rep* **13**, 633 (2023).

824 52. Haverkamp, S., Grünert, U. & Wassle, H. The cone pedicle, a complex synapse in the
825 retina. *Neuron* **27**, 85-95 (2000).

826 53. Grabner, C.P*., et al.* Mechanisms of simultaneous linear and nonlinear computations at the
827 mammalian cone photoreceptor synapse. *Nature communications* **14**, 3486 (2023).

54. Herr, S.*, et al.* Cone synapses in macaque fovea: II. Dendrites of OFF midget bipolar cells exhibit Inner Densities similar to their Outer synaptic Densities in basal contacts with cone terminals. *Visual neuroscience* **28**, 17-28 (2011).

55. Strettoi, E., Raviola, E. & Dacheux, R.F. Synaptic connections of the narrow-field, bistratified rod amacrine cell (AII) in the rabbit retina. *J.Comp.Neurol.* **325**, 152-168 (1992).

56. Strettoi, E., Masri, R.A. & Grünert, U. AII amacrine cells in the primate fovea contribute to photopic vision. *Sci Rep* **8**, 16429 (2018).

57. Wässle, H., Grünert, U., Chun, M.H. & Boycott, B.B. The rod pathway of the macaque monkey retina: Identification of AII-amacrine cells with antibodies against calretinin. *J.Comp.Neurol.* **361**, 537-551 (1995).

58. Grünert, U. Anatomical evidence for rod input to the parvocellular pathway in the visual system of the primate. *Eur.J.Neurosci.* **9**, 617-621 (1997).

59. O'Brien, J.J., Chen, X., Macleish, P.R., O'Brien, J. & Massey, S.C. Photoreceptor coupling mediated by connexin36 in the primate retina. *J Neurosci* **32**, 4675-4687 (2012).

60. Hornstein, E.P., Verweij, J. & Schnapf, J.L. Electrical coupling between red and green cones in primate retina. *Nature neuroscience* **7**, 745-750 (2004).

61. Li, W. & DeVries, S.H. Separate blue and green cone networks in the mammalian retina. *Nature neuroscience* **7**, 751-756 (2004).

62. Kim, Y.J., Packer, O. & Dacey, D.M. A circuit motif for color in the human foveal retina. *Proceedings of the National Academy of Sciences of the United States of America* **121**, e2405138121 (2024).

63. Kolb, H., Goede, P., Roberts, S., McDermott, R. & Gouras, P. Uniqueness of the S-cone pedicle in the human retina and consequences for color processing. *J.Comp.Neurol.* **386**, 443-460 (1997).

852 64. Tsukamoto, Y., Masarachia, P., Schein, S.J. & Sterling, P. Gap junctions between the
853 pedicles of macaque foveal cones. *Vision Res.* **32**, 1809-1815 (1992).

854 65. Thoreson, W.B. & Mangel, S.C. Lateral interactions in the outer retina. *Progress in retinal*
855 *and eye research* **31**, 407-441 (2012).

856 66. Crook, J.D., Manookin, M.B., Packer, O.S. & Dacey, D.M. Horizontal cell feedback without
857 cone type-selective inhibition mediates "red-green" color opponency in midget ganglion
858 cells of the primate retina. *J Neurosci* **31**, 1762-1772 (2011).

859 67. Wool, L.E.*, et al.* Nonselective Wiring Accounts for Red-Green Opponency in Midget
860 Ganglion Cells of the Primate Retina. *J Neurosci* **38**, 1520-1540 (2018).

861 68. Martin, P.R., Blessing, E.M., Buzas, P., Szmajda, B.A. & Forte, J.D. Transmission of colour
862 and acuity signals by parvocellular cells in marmoset monkeys. *J Physiol* **589**, 2795-2812
863 (2011).

864 69. Goodchild, A.K., Chan, T.L. & Grünert, U. Horizontal cell connections with short-
865 wavelength-sensitive cones in macaque monkey retina. *Vis. Neurosci.* **13**, 833-845 (1996).

866 70. Dacey, D.M., Lee, B.B., Stafford, D.K., Pokorny, J. & Smith, V.C. Horizontal cells of the
867 primate retina: cone specificity without spectral opponency. *Science* **271**, 656-659 (1996).

868 71. Chan, T.L. & Grünert, U. Horizontal cell connections with short wavelength-sensitive cones
869 in the retina: A comparison between New World and Old World primates. *J.Comp.Neurol.*
870 **393**, 196-209 (1998).

871 72. Della Santina, L.*, et al.* Glutamatergic Monopolar Interneurons Provide a Novel Pathway of
872 Excitation in the Mouse Retina. *Current biology : CB* **26**, 2070-2077 (2016).

873 73. Lee, S.C., Weltzien, F., Madigan, M.C., Martin, P.R. & Grünert, U. Identification of AII
874 amacrine, displaced amacrine, and bistratified ganglion cell types in human retina with
875 antibodies against calretinin. *J Comp Neurol* **524**, 39-53 (2016).

876 74. Demb, J.B. & Singer, J.H. Intrinsic properties and functional circuitry of the AII amacrine
877 cell. *Visual neuroscience* **29**, 51-60 (2012).

878 75. Diamond, J.S. Inhibitory Interneurons in the Retina: Types, Circuitry, and Function. *Annu*
879 *Rev Vis Sci* **3**, 1-24 (2017).

880 76. Manookin, M.B., Beaudoin, D.L., Ernst, Z.R., Flagel, L.J. & Demb, J.B. Disinhibition
881 combines with excitation to extend the operating range of the OFF visual pathway in
882 daylight. *J Neurosci* **28**, 4136-4150 (2008).

883 77. Peterson, B.B. & Dacey, D.M. Morphology of wide-field, monostratified ganglion cells of
884 the human retina. *Visual neuroscience* **16**, 107-120 (1999).

885 78. Peterson, B.B. & Dacey, D.M. Morphology of wide-field bistratified and diffuse human
886 retinal ganglion cells. *Visual neuroscience* **17**, 567-578 (2000).

887 79. Wassle, H., Puller, C., Muller, F. & Haverkamp, S. Cone contacts, mosaics, and territories
888 of bipolar cells in the mouse retina. *J Neurosci* **29**, 106-117 (2009).

889 80. Cowan, C.S.*, et al.* Cell Types of the Human Retina and Its Organoids at Single-Cell
890 Resolution. *Cell* **182**, 1623-1640 e1634 (2020).

891 81. Puthussery, T., Venkataramani, S., Gayet-Primo, J., Smith, R.G. & Taylor, W.R. NaV1.1
892 channels in axon initial segments of bipolar cells augment input to magnocellular visual
893 pathways in the primate retina. *J Neurosci* **33**, 16045-16059 (2013).

894 82. Tsukamoto, Y. & Omi, N. OFF bipolar cells in macaque retina: type-specific connectivity in
895 the outer and inner synaptic layers. *Frontiers in neuroanatomy* **9**, 122 (2015).

896 83. Masri, R.A., Grünert, U. & Martin, P.R. Analysis of Parvocellular and Magnocellular Visual
897 Pathways in Human Retina. *J Neurosci* **40**, 8132-8148 (2020).

898 84. Wang, A.Y.M.*, et al.* An ON-type direction-selective ganglion cell in primate retina. *Nature*
899 **623**, 381-386 (2023).

900 85. Shevell, S.K. & Martin, P.R. Color opponency: tutorial. *Journal of the Optical Society of*
901 *America. A, Optics, image science, and vision* **34**, 1099-1108 (2017).

902 86. Stockman, A. & Brainard, D.H. Color Vision Mechanisms. in *OSA Handbook of Optics* (ed.
903 M. Bass) 11.11-11.104 (McGraw-Hill, New York, 2010).

904 87. Hsu, A., Smith, R.G., Buchsbaum, G. & Sterling, P. Cost of cone coupling to trichromacy in
905 primate fovea. *Journal of the Optical Society of America. A, Optics, image science, and*
906 *vision* **17**, 635-640 (2000).

907 88. DeVries, S.H., Qi, X., Smith, R., Makous, W. & Sterling, P. Electrical coupling between
908 mammalian cones. *Current biology : CB* **12**, 1900-1907 (2002).

909 89. Popovych, S.*, et al.* Petascale pipeline for precise alignment of images from serial section
910 electron microscopy. *Nature communications* **15**, 289 (2024).

911 90. Lowe, D.G. Object recognition from local scale-invariant features. in *Proceedings of the*
912 *Seventh IEEE International Conference on Computer Vision* 1150-1157 (IEEE, Kerkyra,
913 Greece, 1999).

914 91. Saalfeld, S., Fetter, R., Cardona, A. & Tomancak, P. Elastic volume reconstruction from
915 series of ultra-thin microscopy sections. *Nature methods* **9**, 717-720 (2012).

916 92. Consortium, T.M.*, et al.* Functional connectomics spanning multiple areas of mouse visual
917 cortex. *bioRxiv*, 2021.2007.2028.454025 (2023).

918 93. Lee, K., Zung, J., Li, P.H., Jain, V. & Seung, H.S. Superhuman accuracy on the SNEMI3D
919 connectomics challenge. *arXiv* **preprint arXiv:1706.00120** (2017).

920 94. Lee, K., Lu, R., Luther, K. & Seung, H.S. Learning and Segmenting Dense Voxel
921 Embeddings for 3D Neuron Reconstruction. *IEEE Trans Med Imaging* **40**, 3801-3811
922 (2021).

95. Macrina, T.*, et al.* Petascale neural circuit reconstruction: automated methods. *bioRxiv*, 2021.2008.2004.455162 (2021).

96. Dorkenwald, S.*, et al.* CAVE: Connectome Annotation Versioning Engine. *Nature methods* (2025).

97. Maitin-Shepard, J.*, et al.* google/neuroglancer. (2021).

98. Boycott, B.B. & Wässle, H. Morphological classification of bipolar cells of the primate retina. *Eur.J.Neurosci.* **3**, 1069-1088 (1991).

99. Wässle, H. & Boycott, B.B. Functional architecture of the mammalian retina. *Physiol.Rev.* **71**, 447-480 (1991).

100. Turner, N.L.*, et al.* Synaptic Partner Assignment Using Attentional Voxel Association Networks. in *IEEE 17th International Symposium on Biomedical Imaging (ISBI)* 1-5 (2020).

101. Lu, R., Zlateski, A. & Seung, H.S. Large-scale image segmentation based on distributed clustering algorithms. *arXiv* **arXiv.** http://arxiv.org/abs/2106.10795 **[cs.CV]**, 1-8 (2021).